Silkworm spinning: the programmed self-assembly from

natural silk fibroin to superfibre

Kai Song[1,2], Yejing Wang[1], Wenjie Dong[2], Zhenzhen Li[1], Huawei He[1,3,4*], Ping Zhu[2,5*], Qingyou Xia[1,3*]

[1] State Key Laboratory of Silkworm Genome Biology, Biological Science Research Center, Southwest University, Beibei, Chongqing, 400715, China

[2] National Laboratory of Biomacromolecules, CAS Center for Excellence in Biomacromolecules, Institute of Biophysics, Chinese Academy of Sciences, Beijing 100101, China

[3] Chongqing Key Laboratory of Sericultural Science, Chongqing Engineering and Technology Research Center for Novel Silk Materials, Chongqing 400715, China

[4] Chongqing Key Laboratory of Soft-Matter Material Chemistry and Function Manufacturing, Chongqing 400715, China

[5] University of Chinese Academy of Sciences, Beijing, 100049, China

*Correspondence to: Huawei He (hehuawei@swu.edu.cn), Ping Zhu (zhup@ibp.ac.cn) & Qingyou Xia (xiaqy@swu.edu.cn)

Abstract: Silkworm silk is one of the best natural protein fibers spun by the silkworm at ambient temperature and pressure using aqueous silk protein solution. It is a great challenge to reproduce high-performance artificial fibers comparable to natural silk by bionics for the incomplete understanding of silkworm spinning mechanism, especially the structure and assembly of natural silk fibroin (NSF) in the silk gland. Here, we studied the structure and assembly of NSF with the assistance of amphipol and digitonin. Our results showed NSFs were present as nanofibrils primarily composed of random coils in the silk gland. Metal ions were vital for the formation of NSF nanofibrils. The successive decrease in pH from posterior silk gland (PSG) to anterior silk gland (ASG) resulted in a gradual increase in NSF hydrophobicity. NSF nanofibrils were randomly arranged from PSG to ASG-1, and then self-assembled into herringbone-like patterns near the spinneret (ASG-2) ready for silkworm spinning. Our study reveals the mechanism by which silkworms cleverly utilize metal ions and pH gradient in the silk gland to drive the programmed self-assembly of NSF from disordered nanofibrils to anisotropic liquid crystalline spinning dope (herringbone-like patterns) for silkworm spinning, thus providing novel insights into silkworm/spider spinning mechanism and bionic creation of high-performance fibers.

Main text

Silkworm silk is one of the best protein fibers in nature by far, which has been utilized by humans for more than 5,000 years as a traditional raw material of textiles. More than 100,000 tons of silk are produced in the world each year (*1*). Sericulture is the main source of family income for millions of farmers in Asia. Today, silk has shown great potentials in flexible electronics, biomedicine and other fields as a new type of material (*2-6*). In addition to silkworm silk, spider dragline silk has also attracted increasing interest, as its comprehensive properties are superior to those of any known synthetic fiber (*2, 7, 8*). However, the commercial era of spider silk has not yet come as spiders are difficult to be domesticated.

It is of great significance to resolve silkworm/spider spinning mechanism for bionics. To date, two models, liquid crystalline spinning (*9*) and micelle models (*10*), have been proposed. The

42   major difference lies in the understanding of silk protein (natural silk fibroin, NSF) structure and
43   assembly *in vivo*. The former suggests that silk protein forms liquid crystalline (*11-13*), while the
44   latter claims that silk protein is present as micelles for its amphiphilic primary sequence (*10, 14,*
45   *15*). NSF is stable at 15-30% (w/v) concentrations without precipitation *in vivo* (*2, 16, 17*),
46   whereas it readily transforms from random coil to β-sheet structure *in vitro*, resulting in protein
47   precipitation (*18*). NSF also forms a left-handed 3/2 helix structure specifically at the air-water
48   interface (*19*). Although sericin may protect regenerated silk fibroin (RSF) from aggregation (*20*),
49   it remains unclear how to keep NSF stable *in vitro*. Thus, studying the structure and assembly of
50   NSF *in vivo* is extremely challenging.

51   Here, we found amphipol and digitonin could keep NSF stable *in vitro* through large-scale
52   screening, and then studied the structure and assembly of NSF *in vivo* using metal shadowing,
53   analytical ultracentrifugation (AUC), fluorescence and circular dichroism (CD) spectroscopy.
54   Our results showed from posterior silk gland (PSG) to anterior silk gland (ASG), NSFs were
55   present as nanofibrils predominantly composed of random coils. Metal ions were crucial for the
56   formation of NSF nanofibrils. NSF nanofibrils were randomly distributed in the lumen from PSG
57   to ASG-1. The hydrophobicity of NSF gradually increased with the decrease of pH from PSG to
58   ASG. Near the spinneret, NSFs self-assembled to form herringbone-like patterns (anisotropic
59   liquid crystalline) ready for silkworm spinning.

Digitonin/amphipol could stabilize NSF *in vitro*

61   Large-scale screening showed that membrane scaffold protein MSP1D1 could improve NSF
62   stability from 144 h to 240 h *in vitro* in a concentration-dependent manner. In contrast, BSA
63   decreased NSF stability from 144 h to 96 h (Fig. 1A). MSP1D1 is known as a genetically
64   engineered protein mimicking apolipoprotein A-1 (APOA-1) for the structural study of
65   membrane proteins (*21*). Both APOA and APOE belong to the apolipoprotein family. APOE
66   regulates amyloid-β plaques in the brain of Alzheimer's patients (*22*). Inspired by the
67   amphiphilicity of MSP1D1, we found amphipol and digitonin were similar to MSP1D1, which
68   could keep NSF stable for 336 h without precipitation (Fig. 1B). Digitonin did not change the
69   secondary structure of NSF (Fig. 1C). Indeed, it stabilized the secondary structure of NSF (Fig.
70   1D) without altering its state (Fig. 1E). In contrast, NSF transformed rapidly from random coil to
71   β-sheet structure in the absence of digitonin *in vitro* (Fig. 1F), leading to protein precipitation
72   (Fig. 1G). Amphipol was not suitable in CD study for high background noise, although it could
73   also stabilize NSF *in vitro*.

NSFs are present as nanofibrils composed of random coils in the silk gland

75   With the aid of amphipol/digitonin, we studied the components and properties of NSF. Blue
76   native polyacrylamide gel electrophoresis (BN-PAGE, 3-16%) and SDS-PAGE (4-16%) showed
77   NSF was a macromolecular complex containing four subunits (Fig. 2A), which were further
78   identified as fibroin heavy chain (Fib-H), fibroin light chain (Fib-L), P25 and P25-like by mass
79   spectrometry, respectively (Extended Data Fig. 1).

80   CD spectra suggested the secondary structure of NSF consisted mainly of random coils and a
81   small number of α-helices from PSG to ASG (Fig. 2B), where NSF from ASG was purified by
82   ions exchange and size exclusion chromatography (Extended Data Fig. 2). RSF was also mainly
83   composed of random coils (Extended Data Fig. 3), which did not change over time under
84   different pH (Extended Data Fig. 4). However, the negative cotton effect of RSF completely
85   disappeared at 222 nm (Extended Data Fig. 3), indicating the difference between NSF and RSF.

86   AUC showed that the sedimentation coefficients of NSF from PSG, posterior of MSG
87   (PMSG), middle of MSG (MMSG) and anterior of MSG (AMSG) were 5.788 S, 5.766 S, 5.798
88   S and 5.862 S, and the corresponding friction ratios were 4.088, 4.145, 3.982 and 4.056 (Fig. 2C),
89   respectively. Friction ratios indicated that NSF has a large axial (length-to-width) ratio, implying
90   it may be a fibrous protein. The sedimentation coefficients were very close, indicating NSFs are
91   almost identical from PSG to AMSG.

92   Metal shadowing showed that NSFs were present as nanofibrils without morphological
93   differences from PSG to ASG (Fig. 2D), which was in line with AUC analysis. Cryogenic
94   transmission electron microscopy (Cryo-TEM) further confirmed the formation of NSF
95   nanofibrils (Extended Data Fig. 5).

Metal ions induce the formation of NSF nanofibrils

97   NSF is regarded as a rod-like structure formed by non-covalent aggregation of globular fibroin
98   protein (*23-25*). However, even after incubation with 8 M urea, 2% Triton X-100 and 15 mM
99   dithiothreitol (DTT) for 18 h at 25ºC, NSFs were still present as nanofibrils without the
100 appearance of globules (Extended Data Fig. 6, A and B), suggesting NSF are not aggregates of
101 globular protein.

102 Metal shadowing showed that NSF itself did not form nanofibrils in water, while formed
103 nanofibrils in 50 mM NaCl, which disappeared again after dialysis (Fig. 3A). Hence, we
104 investigated the effects of metal ions on NSF nanofibrils. At 1 mM, Na^+ and K^+ induced NSF to
105 form immature fibrous-like structure (Fig. 3B, a and b), while Ca^{2+} and Mg^{2+} induced NSF to
106 assemble into nanofibrils (Fig. 3B, c and d). At 2.5 mM, Na^+ and K^+ further induced NSF to
107 assemble into nanofibrils (Fig. 3B, e and f). Once the nanofibrils were formed, they did not
108 change with increasing metal ions concentration, even the concentration increased up to 300 mM
109 (Fig. 3B, g to p).

110 Dynamic light scattering (DLS) showed that the hydrodynamic radius and polydispersion
111 coefficient of NSF were 21 nm and 20.5% in 50 mM NaCl, respectively. After dialysis with
112 water, the hydrodynamic radius slightly decreased to 18.4 nm, and the polydispersion coefficient
113 was multimodal (Extended Data Fig. 6C). No spherical NSF particles with uniform size and
114 smaller hydrodynamic radius appeared after dialysis, suggesting that NSF nanofibrils are not
115 assembled by the aggregation of globular fibroin molecules. The results suggested metal ions are
116 necessary for the formation of NSF nanofibrils. The assembly of NSF nanofibrils induced by
117 metal ions is similar to that of chromatin (*26*).

The decrease of pH improves NSF hydrophobicity

119 It is known that the pH in the lumen of silk gland of both silkworms (*27*) and spiders (*28, 29*)
120 continuously decreases from PSG to ASG, which could be mimicked by continuously decreasing
121 pH from 8.0 to 4.8 within 12 h *in vitro* (Fig. 4A). CD spectra showed that pH decreasing did not
122 change the random coil structure of NSF (Fig. 4B), which was consistent with the random coil
123 structure of NSF observed from different segments of the silk gland (Fig. 2B).

124 ANS fluorescence spectra showed that pH decreasing induced a gradual blue-shift of the
125 maximum emission peak (λmax, 507 nm) of NSF (Fig. 4C), indicating a gradual exposure of
126 NSF hydrophobic residues and an increase of NSF hydrophobicity. Similarly, the λmax of RSF
127 gradually blue-shifted with the decrease of pH (Extended Data Fig. 7), indicating pH decreasing
128 improves RSF hydrophobicity, which was in line with the effect of pH on NSF.

129   The random coil structure of NSF was stable in pH 4.8-5.6 within 160 h, however, it gradually
130   transformed into β-sheet structure in pH 6.0-8.0. Increasing pH promoted the transition of
131   random coil to β-sheet structure of NSF (Fig. 4D). The results suggested that the decrease of pH
132   from PSG to ASG does not change the random coil structure of NSF, but results in the exposure
133   of the hydrophobic residues, thus improving the hydrophobicity of NSF.

134 **NSFs self-assemble into herringbone-like patterns near the spinneret**

135   It is not yet clear where the liquid crystalline of silk protein is formed in the current liquid
136   crystalline model (*9, 11, 30, 31*). To address this problem, the orientation of NSF was observed
137   in solution and *in situ* in the spinning dope by metal shadowing, respectively (Extended Data Fig.
138   8). The results showed NSFs were present as nanofibrils randomly arranged in solution. While
139   the concentration was higher than 0.15 mg·mL^{-1}, NSF nanofibrils were tightly stacked with
140   random arrangement, and did not change with the increase of NSF concentration (Fig. 5A, a to d).

141   From PSG to ASG-1 (Fig. 5B), most of NSF nanofibrils were tightly stacked with isotropic
142   orientation (Fig. 5C, a to d), which was consistent with the orientation of NSF nanofibrils in
143   solution (Fig. 5A, c and d). However, a small number of NSF nanofibrils formed an ordered
144   arrangement (Extended Data Fig. 9), which is consistent with the observation of Inoue *et al* (*32*).
145   Interestingly, the long-range ordered molecular alignment of NSF nanofibrils was not observed
146   in the ultra-thin section of ASG-1 (Extended Data Fig. 10), but near the spinneret of ASG-2,
147   where NSF nanofibrils self-assembled into herringbone-like patterns, with the long axes of
148   adjacent molecules aligned parallel to each other (Fig. 5D). The herringbone-like patterns were
149   further packed together to form the spinning dope (Fig. 5E). The results indicated that NSFs are
150   randomly arranged in the lumen from PSG to ASG-1 as isotropic nanofibrils, and self-assemble
151   to form herringbone-like patterns at ASG-2 parallel to the flow direction, which are further
152   packed to form the liquid-crystalline spinning dope with obvious birefringence (*30*).

153 **Discussion**

154   Understanding the structure and assembly of NSF in the silk gland is vital to reveal silkworm
155   natural spinning mechanism. However, it is a great challenge to study the structure and assembly
156   of NSF as it is prone to aggregation *in vitro*. Although RSF is fairly stable *in vitro* (*33*), it has
157   different rheological behaviors (*34, 35*) and structural properties from NSF (Fig. 4, B and D and
158   Extended Data Fig. 3 and 4). Thus, RSF is not an ideal alternative to NSF.

159   To better study the structure and assembly of NSF, we screened and found digitonin and
160   amphipol could stabilize NSF structure *in vitro* (Fig. 1). Digitonin and amphipol likely interact
161   with NSF through hydrophobic interactions, thus preventing NSF aggregation by shielding the
162   hydrophobic regions of NSF. Although it remains unclear how spiders and silkworms keep high
163   concentrations of silk protein stable *in vivo* (*16, 18, 36*), our results establish a fundamental basis
164   for studying the structure and assembly of NSF.

165   The current silk spinning models have shown different understanding on the assembly of silk
166   protein. The micelle model suggests NSFs form micelles (100-200 nm) in solution. With the
167   increase of NSF concentration, micelles coalesce into larger globules (0.8-15 μm), which are
168   further aligned to form fibers under the action of shearing force (*10, 16, 39*). However, the liquid
169   crystalline model indicates the spinning dope in the spider gland and duct forms a nematic phase
170   consisting of rod-like structures, which are essentially aggregates of spherical silk protein (*9, 23*).

171   Previous evidences show NSF is a large molecular complex (2.3 MDa) composed of Fib-H,
172   Fib-L and P25 as a molar ratio of 6:6:1 (*37*) with a sedimentation coefficient of 10 s (*38*). Here,
173   we identified a new component P25-like in NSF, and demonstrated that NSFs are present as
174   nanofibrils with a sedimentation coefficient of about 5.8 S and a friction ratio of about 4.0 both
175   *in vitro* (Fig. 2, C and D and Extended Data Fig. 3) and *in vivo* (Fig. 5C, a to d). Metal ions are
176   essential for the formation of NSF nanofibrils (Fig. 3A).

177   Vollrath *et al.* propose the liquid crystalline spinning model (*9*) based on the birefringence of
178   the spinning dope of spiders (*13*) and silkworms (*11*). However, it is not clear whether the liquid
179   crystalline phase is inherent in the silk gland (*9, 11*), or caused by the shearing force during
180   silkworm spinning (*30*). Kerkam *et al.* indicate that liquid crystals are formed after silk protein
181   out of the silk gland but prior to the formation of silk fiber (*31*). Inspired by the discovery of
182   graphene (*40*), we peeled NSF carefully from the spinning dope without altering its orientation,
183   and then determined the molecular orientation of NSF nanofibrils *in situ* in the spinning dope.
184   Metal shadowing showed that NSF nanofibrils are randomly arranged with isotropic orientation
185   from PSG to ASG-1 (Fig. 5C, a to d). Interestingly, NSF nanofibrils self-assemble into
186   herringbone-like patterns with long-range ordered alignment and anisotropic orientation at ASG-
187   2 (Fig. 5, D and E), where silk proteins show obvious birefringence (*30*), indicating NSF
188   nanofibrils form anisotropic liquid crystalline phase in the spinning dope at ASG-2. Our results
189   not only provide direct evidence for the presence of liquid crystalline phase *in vivo*, but also
190   clearly indicate the composition and location of liquid crystalline phase.

191   The liquid crystalline model suggests NSF forms supramolecular rod-like structures assembled
192   by aggregation of globular silk protein (*23*), however, NSF nanofibrils are very stable without
193   depolymerization into globules even treated by 8 M urea, 2% Triton X-100 and 15 mM DTT at
194   25ºC for 18 h (Extended Data Fig. 6, A and B). DLS indicated NSF nanofibrils may disassemble
195   to form intertwined peptide chains after dialysis with water, rather than globules (Extended Data
196   Fig. 6C).

197   Our results strongly support that NSFs form nanofibrils instead of the assembly of globules in
198   the silk gland, which are different from the micelles/globules in the micelles model (*10, 16, 39*)
199   and the supramolecular rod-like aggregates of globular silk protein in the liquid crystalline model
200   (*23*). In line with the nanofibrils previously observed in silk fibers (*41-43*), our results provided
201   direct evidence that silk fibers are assembled from nanofibrils.

202   Although acidification induces the transformation of spider silk protein from random coil to β-
203   sheet structure (*29, 44*), our study suggested that NSFs from different segments of the silk gland
204   are mainly composed of random coil (Fig. 2B), and pH decreasing does not change the random
205   coil structure of NSF (Fig. 4B), indicating acidification (pH decreasing) does not induce the
206   formation of β-sheet structure of NSF *in vivo*. Surprisingly, the β-sheet crystallinity of silk fiber
207   is very small produced by silkworms at low humidity (*45*), implying that NSF itself does not
208   form β-sheet structure *in vivo*. Therefore, the β-sheet structure of silk fiber is most likely formed
209   after NSF is spun out of the silk gland.

210   Dehydration caused by shearing force and extensional flow is crucial for silk formation (*9, 30*),
211   as sufficiently high concentration of NSF is the basis for silkworms spinning. Here, we found
212   that pH decreasing improves the hydrophobicity of NSF instead of inducing the formation of β-
213   sheet structure (Fig. 4C), which further triggers the separation of NSF from water, thus
214   promoting the dehydration of NSF and an increase of NSF concentration (*9*). Our study suggests

that the dehydration caused by pH decreasing is likely crucial for the self-assembly of NSF nanofibrils into herringbone-like patterns (anisotropic liquid crystalline phase) and the final formation of silk fiber.

Obviously, good molecular pre-alignment contributes significantly to the toughness of silk fiber (*9*). Unlike the alignment formed by post-spinning stretching in current artificial spinning, this pre-formed highly ordered molecular alignment may explain the higher toughness of natural silk compared to artificial silk (*46*), and is likely the basis of spider silk as biological superlens (*47*). Unfortunately, it is still unclear how NSF nanofibrils self-assemble into herringbone-like patterns, which is likely initiated by the dimerization of the N-terminal domain of silk protein in response to pH decreasing (*48-50*), and related to NSF concentration (*11, 31*) and shearing force (*30*).

In summary, our results suggest NSFs are present as nanofibrils mainly composed of random coils in the silk gland. Metal ions are indispensable for the formation of NSF nanofibrils. The successive pH decreasing from PSG to ASG improves the hydrophobicity and concentration of NSF rather than inducing the formation of β-sheet structure of NSF. NSF nanofibrils are randomly arranged from PSG to ASG-1, and self-assemble into anisotropic liquid crystalline spinning dope (herringbone-like patterns) at ASG-2 ready for silkworm spinning (Fig. 6). Consequently, silk fibers are formed by the programmed self-assembly of NSF nanofibers undergo an orientation transition from isotropy to anisotropy under the actions of various factors such as decreasing pH gradient, metal ions and shearing force. These findings provide novel insights into silkworm spinning mechanism and biomimetic synthesis of high-performance fibers.

References and Notes:

1. N. V. Padaki, B. Das, A. Basu, "[Advances in understanding the properties of silk]" in *Advances in silk science and technology* (Woodhead Publishing, UK, 2015), pp. 3-4.

2. F. G. Omenetto, D. L. Kaplan, New opportunities for an ancient material. *Science* **329**, 528-531 (2010).

3. D. H. Kim *et al.*, Dissolvable films of silk fibroin for ultrathin conformal bio-integrated electronics. *Nat. Mater.* **9**, 511-517 (2010).

4. C. Guo *et al.*, Thermoplastic moulding of regenerated silk. *Nat. Mater.* **19**, 102-108 (2020).

5. W. Lee *et al.*, A rewritable optical storage medium of silk proteins using near-field nano-optics. *Nat. Nanotechnol.* **15**, 941-947 (2020).

6. U. Shimanovich *et al.*, Silk micrococoons for protein stabilisation and molecular encapsulation. *Nat. Commun.* **8**, 15902 (2017).

7. C. Fu, Z. Shao, V. Fritz, Animal silks: their structures, properties and artificial production. *Chem. Commun. (Cambridge, U. K.)*, 6515-6529 (2009).

8. I. Agnarsson, M. Kuntner, T. A. Blackledge, Bioprospecting Finds the Toughest Biological Material: Extraordinary Silk from a Giant Riverine Orb Spider. *PLoS One* **5**, (2010).

9. F. Vollrath, D. P. Knight, Liquid crystalline spinning of spider silk. *Nature* **410**, 541-548 (2001).

10. H. J. Jin, D. L. Kaplan, Mechanism of silk processing in insects and spiders. *Nature* **424**, 1057-1061 (2003).

11. G. X. Li, T. Y. Yu, Investigation of the liquid-crystal state in silk fibroin. *Makromol. Chem., Rapid Commun.* **10**, 387-389 (1989).

12. P. J. Willcox, S. P. Gido, W. Muller, D. L. Kaplan, Evidence of a cholesteric liquid crystalline phase in natural silk spinning processes. *Macromolecules* **29**, 5106-5110 (1996).

13. D. P. Knight, F. Vollrath, Liquid crystals and flow elongation in a spider's silk production line. *Proc. R. Soc. B*

266, 519-523 (1999).

14. M. Heim, D. Keerl, T. Scheibel, Spider silk: From soluble protein to extraordinary fiber. *Angew. Chem., Int. Ed.* *48*, 3584-3596 (2009).

15. R. Silvers, F. Buhr, H. Schwalbe, The molecular mechanism of spider-silk formation. *Angew. Chem., Int. Ed. 49*, 5410-5412 (2010).

16. E. Atkins, Silk's secrets. *Nature 424*, 1010 (2003).

17. F. Hagn *et al.*, A conserved spider silk domain acts as a molecular switch that controls fibre assembly. *Nature 465*, 239-242 (2010).

18. I. Greving, C. Dicko, A. Terry, P. Callow, F. Vollrath, Small angle neutron scattering of native and reconstituted silk fibroin. *Soft Matter 6*, 4389-4395 (2010).

19. R. Valluzzi, S. P. Gido, W. P. Zhang, W. S. Muller, D. L. Kaplan, Trigonal crystal structure of *Bombyx mori* silk incorporating a threefold helical chain conformation found at the air-water interface. *Macromolecules 29*, 8606-8614 (1996).

20. H. W. Kwak, J. E. Ju, M. Shin, C. Holland, K. H. Lee, Sericin promotes fibroin silk I stabilization across a phase-separation. *Biomacromolecules 18*, 2343-2349 (2017).

21. I. G. Denisov, S. G. Sligar, Nanodiscs for structural and functional studies of membrane proteins. *Nat. Struct. Mol. Biol. 23*, 481-486 (2016).

22. Y. Yamazaki, N. Zhao, T. R. Caulfield, C. C. Liu, G. J. Bu, Apolipoprotein E and Alzheimer disease: pathobiology and targeting strategies. *Nat. Rev. Neurol. 15*, 501-518 (2019).

23. C. Viney, Natural silks : Archetypal supramolecular assembly of polymer fibres. *Supramol. Sci. 4*, 75-81 (1997).

24. T. Y. Lin *et al.*, Liquid crystalline granules align in a hierarchical structure to produce spider dragline microfibrils. *Biomacromolecules 18*, 1350-1355 (2017).

25. S. Ling, C. Li, K. Jin, D. L. Kaplan, M. J. Buehler, Liquid exfoliated natural silk nanofibrils: Applications in optical and electrical devices. *Adv. Mater. (Weinheim, Ger.) 28*, 7783-7790 (2016).

26. S. A. Grigoryev, G. Arya, S. Correll, C. L. Woodcock, T. Schlick, Evidence for heteromorphic chromatin fibers from analysis of nucleosome interactions. *Proc. Natl. Acad. Sci. U. S. A. 106*, 13317-13322 (2009).

27. L. J. Domigan *et al.*, Carbonic anhydrase generates a pH gradient in *Bombyx mori* silk glands. *Insect Biochem. Mol. Biol. 65*, 100-106 (2015).

28. M. Andersson *et al.*, Carbonic anhydrase generates CO_2 and H^+ that drive spider silk formation via opposite effects on the terminal domains. *PLoS Biol. 12*, (2014).

29. C. Dicko, F. Vollrath, J. M. Kenney, Spider silk protein refolding is controlled by changing pH. *Biomacromolecules 5*, 704-710 (2004).

30. T. Asakura *et al.*, Some observations on the structure and function of the spinning apparatus in the silkworm *Bombyx mori*. *Biomacromolecules 8*, 175-181 (2007).

31. K. Kerkam, C. Viney, D. Kaplan, S. Lombardi, Liquid crystallinity of natural silk secretions. *Nature 349*, 596-598 (1991).

32. S. Inoue *et al.*, Nanostructure of natural fibrous protein: In vitro nanofabric formation of *Samia cynthia ricini* wild silk fibroin by self-assembling. *Nano Lett. 3*, 1329-1332 (2003).

33. D. N. Rockwood *et al.*, Materials fabrication from *Bombyx mori* silk fibroin. *Nat. Protoc. 6*, 1612-1631 (2011).

34. D. Porter, F. Vollrath, Silk as a biomimetic ideal for structural polymers. *Adv. Mater. (Weinheim, Ger.) 21*, 487-492 (2009).

35. C. Holland, A. E. Terry, D. Porter, F. Vollrath, Comparing the rheology of native spider and silkworm spinning dope. *Nat. Mater. 5*, 870-874 (2006).

36. E. Pennisi, Untangling spider biology: Genomics begins to unravel the roots of spider diversity and the recipes

of their silk and venom. *Science 358*, 288-291 (2017).

37. S. Inoue *et al.*, Silk fibroin of *Bombyx mori* is secreted, assembling a high molecular mass elementary unit consisting of H-chain, L-chain, and P25, with a 6:6:1 molar ratio. *J. Biol. Chem. 275*, 40517-40528 (2000).

38. Y. Tashiro, E. Otsuki, Studies on posterior silk gland of silkworm *Bombix mori* IV. Ultracentrifugal analyses of native silk proteins, especially fibroin extracted from middle silk gland of mature silkworm. *J. Cell Biol. 46*, 1-& (1970).

39. L. R. Parent *et al.*, Hierarchical spidroin micellar nanoparticles as the fundamental precursors of spider silks. *Proc. Natl. Acad. Sci. U. S. A. 115*, 11507-11512 (2018).

40. K. S. Novoselov *et al.*, Electric field effect in atomically thin carbon films. *Science 306*, 666-669 (2004).

41. N. Du, Z. Yang, X. Y. Liu, Y. Li, H. Y. Xu, Structural origin of the strain-hardening of spider silk. *Adv. Funct. Mater. 21*, 772-778 (2011).

42. S. H. Choi *et al.*, Anderson light localization in biological nanostructures of native silk. *Nat. Commun. 9*, 452 (2018).

43. S. Putthanarat, N. Stribeck, S. A. Fossey, R. K. Eby, W. W. Adams, Investigation of the nanofibrils of silk fibers. *Polymer 41*, 7735-7747 (2000).

44. C. Dicko, J. M. Kenney, D. Knight, F. Vollrath, Transition to a β-sheet-rich structure in spidroin *in vitro*: The effects of ph and cations. *Biochemistry-Us 43*, 14080-14087 (2004).

45. M. Boulet-Audet, C. Holland, T. Gheysens, F. Vollrath, Dry-spun silk produces native-like fibroin solutions. *Biomacromolecules 17*, 3198-3204 (2016).

46. M. Andersson *et al.*, Biomimetic spinning of artificial spider silk from a chimeric minispidroin. *Nat. Chem. Biol. 13*, 262-264 (2017).

47. J. N. Monks, B. Yan, N. Hawkins, F. Vollrath, Z. Wang, Spider silk: Mother nature's bio-superlens. *Nano Lett. 16*, 5842-5845 (2016).

48. Y. X. He *et al.*, N-terminal domain of *Bombyx mori* fibroin mediates the assembly of silk in response to pH decrease. *J. Mol. Biol. 418*, 197-207 (2012).

49. W. A. Gaines, M. G. Sehorn, W. R. Marcotte, Jr., Spidroin N-terminal domain promotes a pH-dependent association of silk proteins during self-assembly. *J. Biol. Chem. 285*, 40745-40753 (2010).

50. G. Askarieh *et al.*, Self-assembly of spider silk proteins is controlled by a pH-sensitive relay. *Nature 465*, 236-238 (2010).

51. Q. Xia, S. Li, Q. Feng, Advances in silkworm studies accelerated by the genome sequencing of *Bombyx mori*. *Annu. Rev. Entomol. 59*, 513-536 (2014).

52. J. Y. Li *et al.*, Comparative proteomic analysis of the silkworm middle silk gland reveals the importance of ribosome biogenesis in silk protein production. *J. Proteomics 126*, 109-120 (2015).

53. T. K. Ritchie *et al.*, Chapter 11 - Reconstitution of membrane proteins in phospholipid bilayer nanodiscs. *Methods Enzymol. 464*, 211-231 (2009).

54. I. Wittig, H. P. Braun, H. Schagger, Blue native PAGE. *Nat. Protoc. 1*, 418-428 (2006).

55. J. D. Griffith, Electron microscopic visualization of DNA in association with cellular components. *Methods Cell Biol. 7*, 129-146 (1973).

347

Fig. 1. Amphiphilic molecules improved the stability of NSF *in vitro*. (A) The changes of UV absorption of NSF (A$_{280}$) over time in the presence of MSP1D1. M, MSP1D1; B, BSA. **(B)** The changes of UV absorption of NSF (A$_{280}$) over time in the presence of different detergents. **(C)** CD spectra of NSF in the presence or absence of digitonin. **(D)** CD spectra of NSF in the presence of digitonin over time. **(E)** The morphology of NSF in the presence of digitonin. The inset showed NSF was stable in the presence of digitonin after 24 h and 264 h, respectively. **(F)** CD spectra of NSF in the absence of digitonin over time. **(G)** The morphology of NSF in the absence of digitonin. The inset showed the aggregation of NSF in the absence of digitonin after 24 h and 264 h, respectively. Scale bar, 200 nm.

348
349
350
351
352
353
354
355
356
357
358
359
360
361
362
363
364
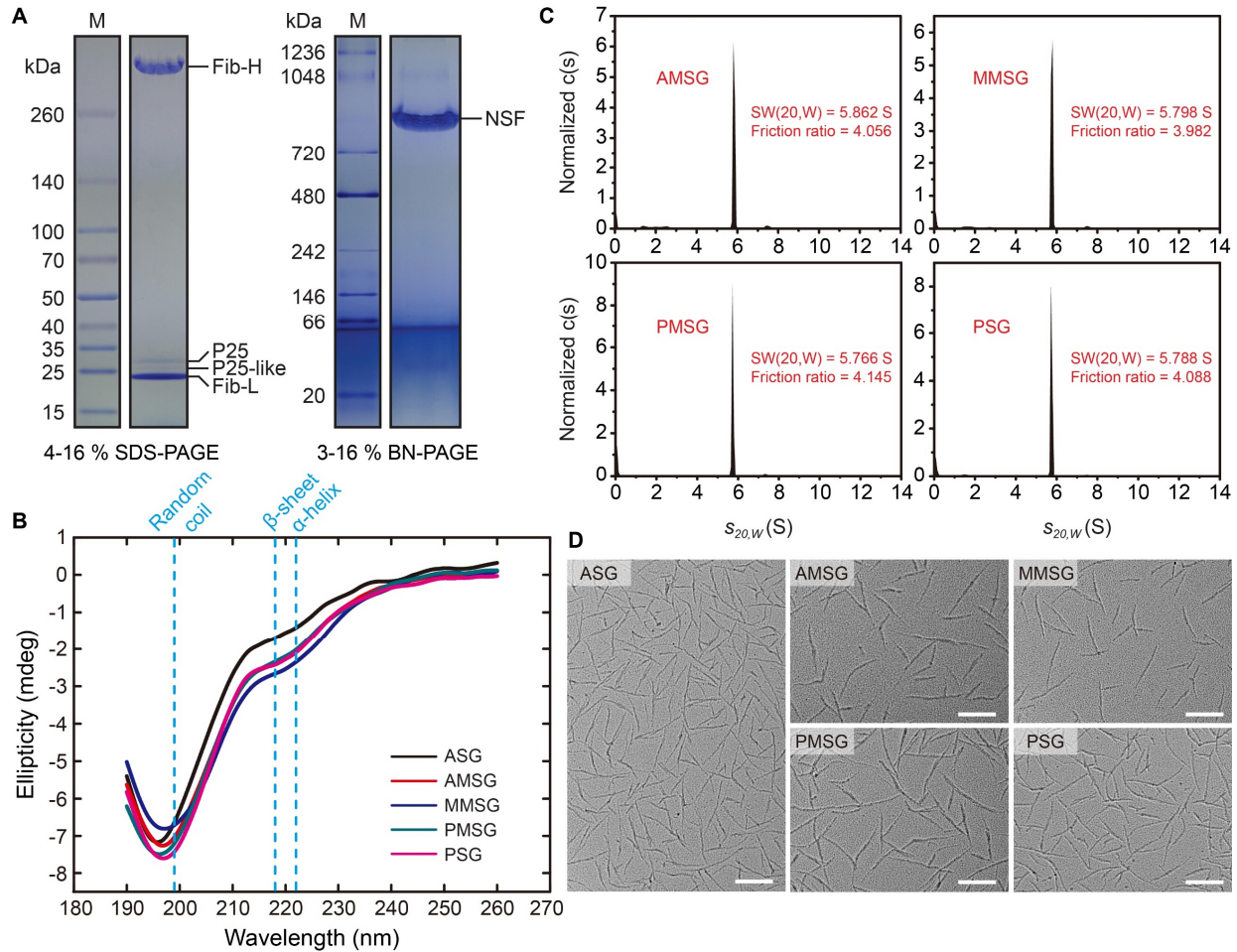
Fig. 2. The components and structure of NSF. **(A)** NSF components analysis. NSF was separated by linear gradient SDS-PAGE gel (4-16%) (left) and BN-PAGE gel (3-16%) (right). **(B)** CD spectra of NSF from PSG, PMSG, MMSG, AMSG, ASG. **(C)** AUC analysis of NSF from PSG, PMSG, MMSG and AMSG. The distributions of normalized c(s) were plotted as the function of the sedimentation coefficients $s_{20,w}$ (S). S, Svedberg (the unit of sedimentation coefficient). **(D)** Metal shadowing of NSF from PSG, PMSG, MMSG, AMSG and ASG. NSF concentration was 0.025 mg·mL^{-1} in 10 mM phosphate buffer. Scale bar, 200 nm.
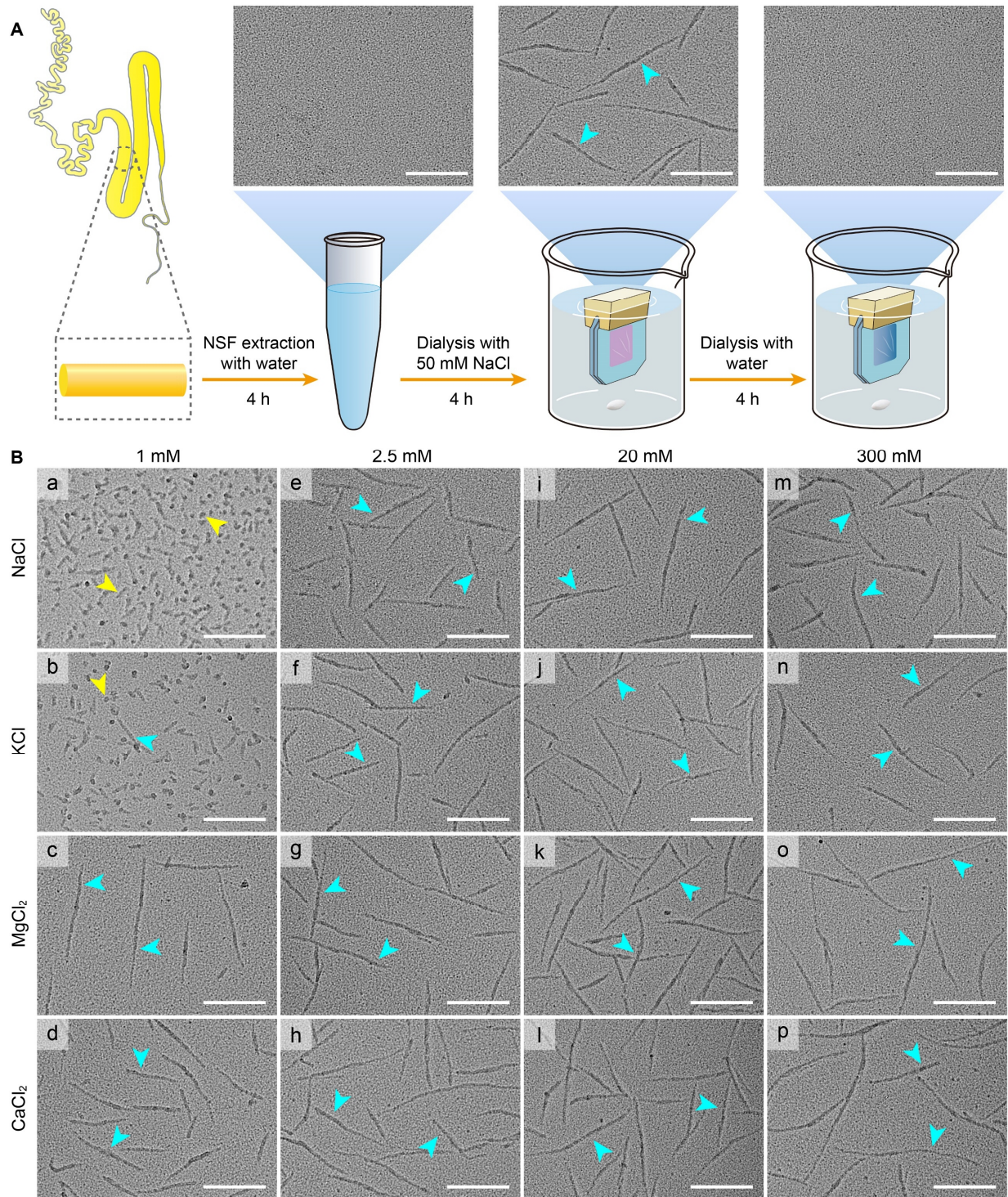
Fig. 3. Effect of metal ions on the formation of NSF nanofibrils. (A) Metal ions induced the formation of NSF nanofibrils. **(B)** Metal shadowing of NSF in the presence of different concentrations of metal ions. Blue and yellow arrows showed the mature NSF nanofibrils and the immature fibrous-like structure, respectively. Scale bar, 200 nm.
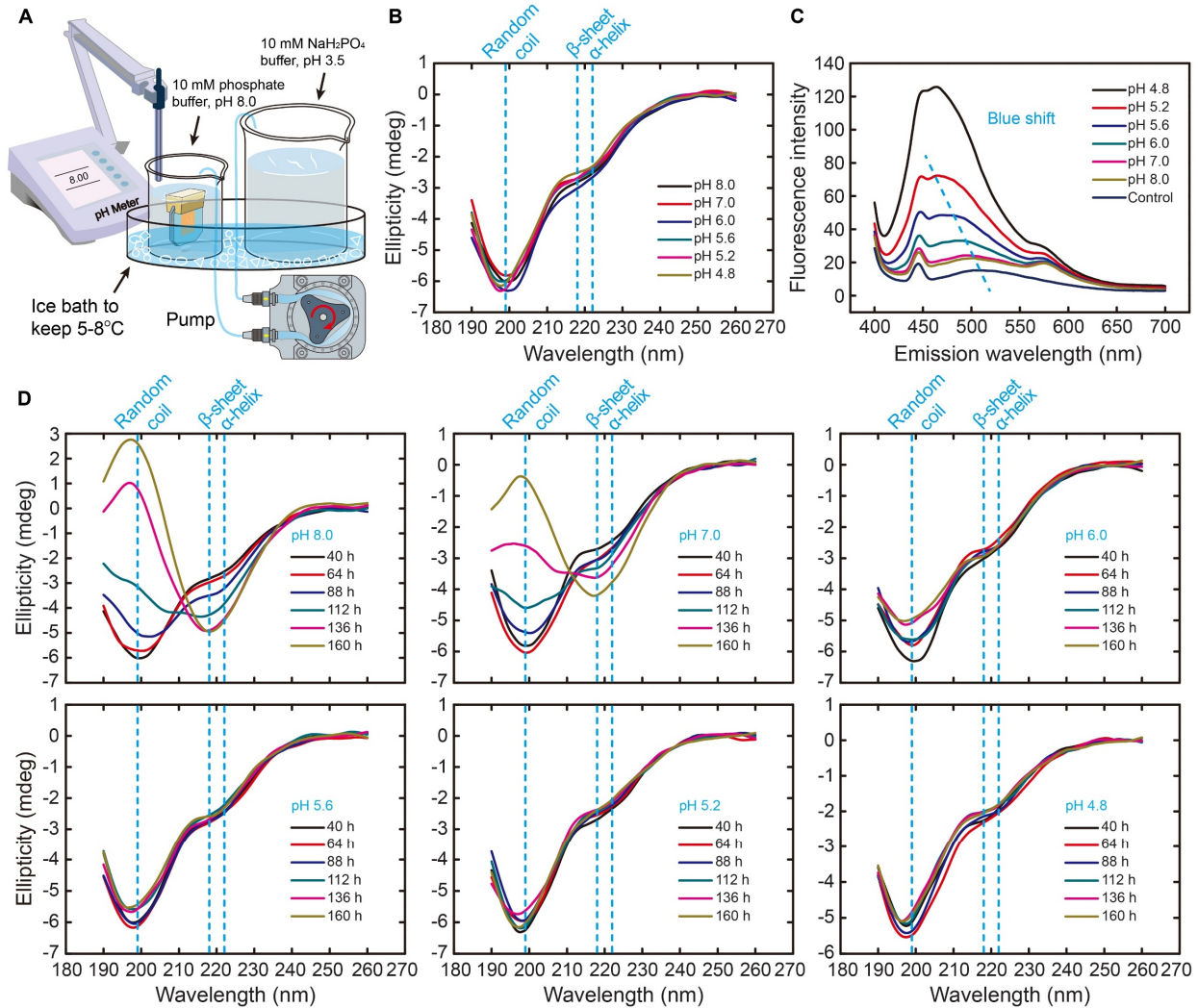
Fig. 4. Effect of pH on the structure of NSF. (A) Schematic diagram of the formation of a continuous decreasing pH gradient. **(B)** CD spectra of NSF under different pH. **(C)** ANS fluorescence spectra of NSF under different pH. The dotted line showed the blue shift of λmax of NSF. **(D)** Effect of pH on CD spectra of NSF over time.

408

409
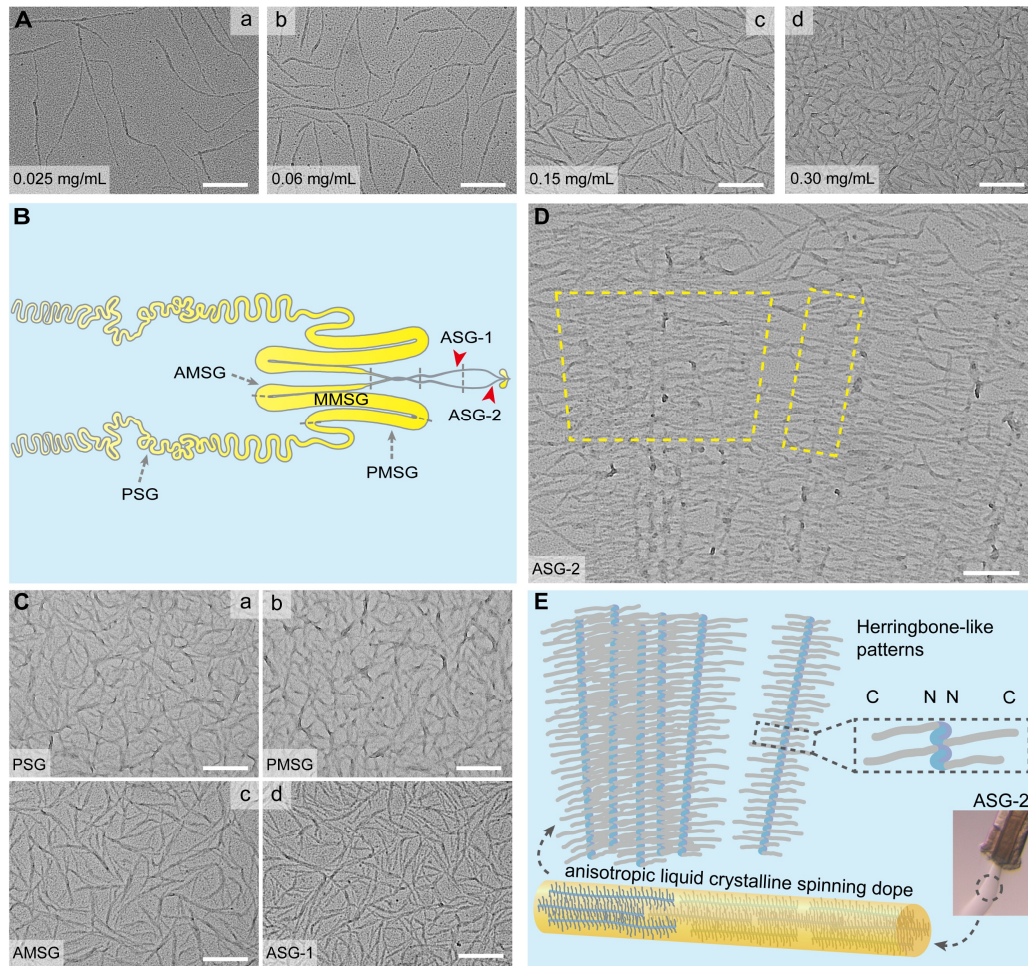
Fig. 5. Metal shadowing showed the arrangement and orientation of NSF nanofibrils. (A) Metal shadowing of different concentrations of NSF in solution. **(B)** Schematic diagram of different divisions of the silk gland. **(C)** Metal shadowing of NSF *in situ* from different divisions of the silk gland. **(D)** Herringbone-like patterns (anisotropic liquid crystalline phase) self-assembled by NSF nanofibrils at ASG-2. The yellow boxes indicate representative herringbone-like patterns. **(E)** Schematic diagram of anisotropic liquid crystalline spinning dope self-assembled by NSF nanofibrils. C and N, the C and N terminal domain of Fib-H, respectively. Scale bar, 200 nm.

410
411
412
413
414
415
416
417
418
419
420
421
422
423
424
425
426
427
428
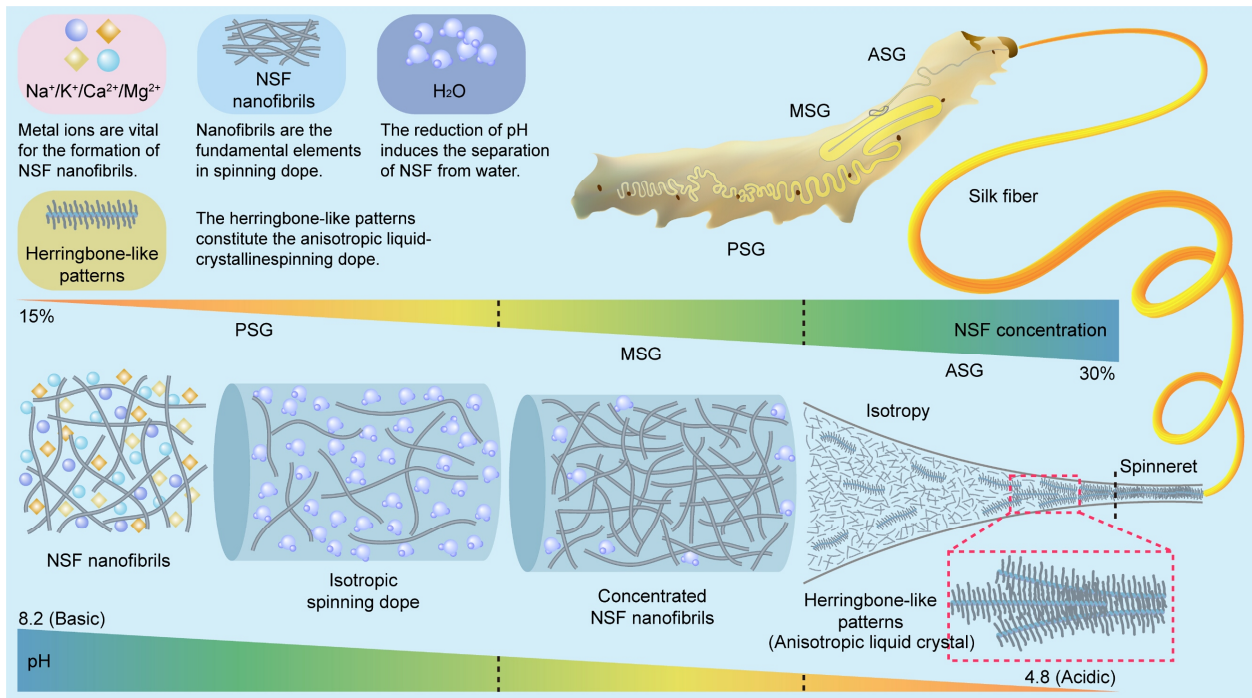
Fig. 6. Schematic illustration of the programmed self-assembly of NSF driven by pH gradient and metal ions in the silk gland of the silkworm. (a) NSF is a soluble macromolecular complex with a sedimentation coefficient of 5.8 S, and present as nanofibrils induced by metal ions in the silk gland. **(b)** From PSG to ASG, NSF is mainly composed of random coils. With the decrease of pH from about 8.2 in PSG to 4.8 in ASG, the hydrophobicity of NSF is gradually enhanced, and NSF concentration increases up to about 30% (w/v). **(c)** Near the spinneret at ASG-2, NSF nanofibrils self-assemble into herringbone-like patterns (anisotropic liquid-crystalline phase) ready for silkworm spinning.

Methods

Isolation and purification of NSF

The silkworm strain Jinsong (*Bombyx mori*), used in this study, was supplied by the State Key Laboratory of Silkworm Genome Biology (Southwest University, Chongqing, China). Silkworm larvae were reared at room temperature until the early wandering stage, then frozen with liquid nitrogen and stored at -80ºC. The silk gland is divided into posterior silk gland (PSG), middle silk gland (MSG) and anterior silk gland (ASG) (*51*). Further, MSG has three sections including posterior of MSG (PMSG), middle of MSG (MMSG) and anterior of MSG (AMSG) (*52*). Silk gland was dissected from the frozen silkworm. Silk protein is composed of fibroin and sericin, and stored in the lumen of silk gland (LSG) after synthesis. Sericin could be easily separated from fibroin as it becomes insoluble after freezing. Therefore, natural silk fibroin (NSF) could be purified from the lumen of PSG, PMSG, MMSG and AMSG, respectively. Ultrapure water was prepared by Milli-Q IQ 7000 (Merck, Germany) and used for all tests.

ASG was collected from two hundred fifty living silkworm larvae at the late wandering stage, and then rinsed twice with phosphate-buffered saline (PBS, pH 7.4) for 5 s each. Next, ASG was submerged into 4 mL buffer I (100 mM NaCl, 20 mM Tris-HCl, 0.5 mM EDTA, pH 7.3) pre-cooled at 4ºC, and carefully sliced into 3-5 mm segments. After incubation on ice for 4 h, NSF was gradually extracted into buffer I. To keep NSF stable, digitonin was added into the supernatant (0.1%, w/v) after centrifugation at 10,000 g at 4ºC for 10 min. Then, the supernatant was incubated with S cation exchange media (200 μL) (Bio-rad, USA) with rotation at 4ºC for 2 h. After centrifugation at 1,000 g at 4ºC for 10 min, the supernatant was then incubated with Q anion exchange media (200 μL) (Bio-rad) at 4ºC for 2 h. Then the media was removed by centrifugation at 10,000 g at 4ºC for 10 min. S and Q media were pre-equilibrated with buffer I, respectively. NSF was further purified from the supernatant by size-exclusion chromatography on a Superdex 200 10/300 GL increase column (GE Healthcare, USA) with 10 mM phosphate buffer (Na_2HPO_4, NaH_2PO_4, pH 8.0) containing 0.015% digitonin. The homogeneity of NSF was assessed by sodium dodecyl sulfate polyacrylamide gel electrophoresis (SDS-PAGE) and Coomassie Brilliant Blue staining (Extended Data Fig. 2). NSF concentration was measured at 280 nm on a NanoDrop 2000C spectrophotometer (Thermo Fisher Scientific, USA). NSF was freshly purified and used immediately to avoid the potential effect of flash-frozen with liquid nitrogen on the structure and properties of NSF.

Preparation of regenerated silk fibroin

Regenerated silk fibroin (RSF) was prepared as previously described (*33*) with minor modifications. Silkworm cocoons were boiled in 0.02 M Na_2CO_3 for 30 min, and then rinsed with water twice to remove soluble sericin from silk fibroin. After drying overnight at room temperature, the degummed silk fiber (silk fibroin) was dissolved in 9 M LiBr (Sangon, China) at 60ºC for 20 min to yield 10% (w/v) RSF solution. RSF was dialyzed against water at 4ºC for 12 h to remove LiBr, and then dialyzed against 10 mM PBS (pH 8.0) at 4ºC for 12 h. After removal of the undissolved aggregates by centrifugation (10,000 g) at 4ºC for 15 min, RSF concentration was determined at 280 nm on a NanoDrop 2000C spectrophotometer (Thermo Fisher Scientific).

Expression and purification of MSP1D1

501   Membrane scaffold protein MSP1D1 was expressed and purified as described (*53*) with minor
502 modifications. In brief, MSP1D1 was expressed in *E. coli* BL21 (DE3) and induced with 1 mM
503 isopropyl β-D-1-thiogalactopyranoside (IPTG) until the OD_{600} of the cells reached 0.6 at 37ºC.
504 After 4 h of induction at 28ºC, the cells were collected and then lysed in 20 mM PBS (pH 7.4)
505 containing 1 mM PMSF and 1% Triton X-100. MSP1D1 was purified using his-tag affinity
506 chromatography after centrifugation at 12,000 g for 30 min at 4ºC, and then dialyzed against 20
507 mM PBS (pH 7.4) at 4ºC for 24 h to remove imidazole. MSP1D1 concentration was measured at
508 280 nm using a calculated extinction coefficient of 21,430 $L·mol^{-1}·cm^{-1}$. MSP1D1 was
509 concentrated to 5 $mg·mL^{-1}$ and stored at -80ºC.
510

Polyacrylamide gel electrophoresis

512   NSF was boiled in reducing buffer for 10 min, and then analyzed by a linear gradient (4-16%)
513 SDS-PAGE gel, which was generated by Hoefer SG 30 gradient maker (Thermo Fisher
514 Scientific). The linear gradient (3-16%) blue native-PAGE (BN-PAGE) gel was cast as witting's
515 protocol (*54*) using Hoefer SG 30 gradient maker. NSF was incubated with amphipol (Anatrace,
516 USA) at a mass ratio of 1:6 at 4ºC for 72 h, then mixed with native-PAGE loading buffer
517 (Invitrogen, USA) and separated by 3-16% BN-PAGE. The molecular weight of NSF was
518 estimated as 445 kDa.
519

Circular dichroism

521   Circular dichroism (CD) spectra were collected from 260 to 190 nm using a 0.1 cm light-path
522 quartz cuvette on a Chirascan Plus spectrometer (Chirascan, UK) with 1 nm bandwidth, 0.5 s
523 response time and 50 $nm·min^{-1}$ scanning speed. NSF was dissolved in 10 mM PBS (pH 8.0) with
524 a final concentration of 0.1 $mg·mL^{-1}$.
525

Sedimentation velocity analytical ultracentrifugation

527   NSF was mixed with amphipol at a mass ratio of 1:6 in buffer II (50 mM NaCl, 50 mM Bis-
528 Tris, 0.5 mM EDTA, pH 7.5) with a final concentration of 0.75 $mg·mL^{-1}$. Amphipol was
529 dissolved in buffer II with the same concentration as the control. After 72 h of incubation at 4ºC,
530 NSF/amphipol (400 μL) and amphipol (400 μL) were loaded into double-sector quartz cells,
531 respectively, mounted into an eight-hole AN-50 Ti rotor, and then centrifuged at 45,000 rpm on
532 ProteomeLab XL-I (Beckman coulter, USA) at 20ºC for 5 h. The absorbance at 280 nm was
533 recorded for sedimentation velocity analytical ultracentrifugation (SV-AUC) analysis. The buffer
534 density, viscosity and partial specific volume of NSF were calculated using SEDNTERP (ver.
535 1.09) to be 1.0018 $g·mL^{-1}$, 1.02298 cP and 0.6945 $cm^3·g^{-1}$, respectively.
536

Metal shadowing

538   Metal shadowing was performed as Griffith's method (*55*), as illustrated in figure. S8. For the
539 metal shadowing of NSF in solution, one droplet of NSF (5 μL, 0.025 $mg·mL^{-1}$) was applied to
540 glow-discharged copper grids for 2 min. Excess NSF was carefully removed by blotting paper.
541 For the metal shadowing of NSF *in situ* in the spinning dope, a glow-discharged copper grid was
542 placed on the spinning dope to touch it gently and carefully with tweezers without moving the
543 copper grip to avoid the possible artifact of NSF stacking. NSF was dehydrated in gradient
544 ethanol (0, 25%, 50%, 75%, 100%) for 4 min each, then shadowed with tungsten by DV-502B
545 high vacuum evaporator (Denton Vacuum, USA) followed by air drying. A tungsten wire (8 cm

16

546 in length) was clamped between two electrodes at a distance of 3.8 cm. The distance of the wire
547 was 9.3 cm from the center of the specimen platform. The angle between the tungsten wire and
548 the sample was about 10°. The total evaporation time was 14.5 min. NSF was kept rotation
549 during the evaporation. Transmission electron microscopy (TEM) was carried out on a Tecnai
550 Spirit (FEI, USA).

Cryogenic transmission electron microscopy
553 NSF was purified from PMSG, and then mixed with amphipol in buffer II at a mass ratio of
554 1:6. The final concentration of NSF was 1.5 mg·mL^{-1}. After 72 h of incubation at 4ºC, the
555 mixture (3 μL) was loaded on a glow-discharged holey grid (GIG, 1.2-1.3, Au), then vitrified by
556 flash plunging the grid into liquid ethane using vitrobot Mark IV (FEI). The blotting time, force
557 level and humidity were set to be 7 s, 0 and 100%, respectively. Cryogenic transmission electron
558 microscopy (Cryo-TEM) was performed on a 200 kV Talos F200C microscope (FEI) equipped
559 with Ceta camera (FEI).

Stability analysis of NSF
562 NSF was purified from PMSG with 20 mM PBS (pH 7.4), and then gently incubated with
563 various detergents at 4ºC. The final concentration of NSF and the detergents was 2.93 mg·mL^{-1}
564 and five folds of critical micelle concentration (CMC), respectively, except amphipol was mixed
565 with NSF at a mass ratio of 3:1 (Extended Data Table 1). NSF was incubated with MSP1D1 and
566 BSA as the same procedures. Here, the concentrations of NSF, MSP1D1 and BSA were 2
567 mg·mL^{-1}, 4 mg·mL^{-1} and 10.56 mg·mL^{-1} (Extended Data Table 2 and 3), respectively. Then, the
568 mixture (8 μL) was collected every 24 h, and centrifuged at 10,000 g at 4ºC for 10 min. The
569 concentration of the supernatant was determined at 280 nm on a NanoDrop 2000C
570 spectrophotometer (Thermo Fisher Scientific) to value the effects of the detergents, MSP1D1
571 and BSA on the stability of NSF. Various detergents and BSA were dissolved in water and 20
572 mM PBS (pH 7.4), respectively, and stored at -20ºC.

Liquid chromatography-tandem mass spectrometry
575 To identify the components of NSF, NSF was separated by a linear 4-16% SDS-PAGE, and
576 then stained with Coomassie light blue. The target bands were excised for alkylation and
577 reduction with dithiothreitol and iodoacetamide (Sigma, USA), respectively, then digested
578 overnight with trypsin (Promega, USA). Next, the in-gel proteins were extracted by successive
579 washing of gel slices with acetonitrile, and then subjected to liquid chromatography-tandem
580 mass spectrometry (LC-MS/MS) using an LTQ Obitrap XL mass spectrometer (Thermo Fisher
581 Scientific) coupled to a RSLC nano-high performance liquid chromatography (Dionex, USA)
582 system. The peptides were loaded onto a self-packing column (inner diameter, 75 μm; length, 15
583 cm) filled with 3 μm ReproSil-Pur C18-AQ resin (Dr. Maisch GmbH, Germany), and then eluted
584 with an organic gradient phase (buffer A: 0.5% formic acid/H$_2$O; buffer B: 0.5% formic
585 acid/acetonitrile) at a flow rate of 300 nL/min for 100 min. The program was set as: 0-77 min, 4%
586 buffer B; 78-82 min, 36% buffer B; 83-90 min, 80% buffer B; 91-100 min, 4% buffer B. The
587 datasets were processed with the Proteome Discoverer program (ver 1.4.0.288, Thermo Fischer
588 Scientific). In general, a mass tolerance of 20 ppm for parent ions, 0.6 Da for fragment ions, two
589 missed cleavages, oxidation of Met (dynamic modification) and carbamidomethyl cysteine (fixed

590 modification) were selected as search matching parameters. The results were evaluated using a
591 percolator node (high-confidence q value, FDR < 0.01) to exclude false positives.
592

ANS fluorescence spectroscopy

594 ANS fluorescence spectra were collected on an F7000 spectrophotometer (Hitachi, Japan) in
595 dark at room temperature using a 1 cm light-path cell. NSF (0.3 nM) was incubated with 3 nM
596 ANS in dark under different pH on ice for 3 h. Then, the samples were excited at 388 nm, and
597 the fluorescence emission spectra were recorded from 400 to 700 nm with a scanning speed of
598 240 nm·min^{-1}. ANS was dissolved in water with a stock concentration of 3 mM.
599

Ultrathin section of ASG

601 ASG (including the spinneret) was carefully dissected from mature fifth instar silkworm larvae
602 to ensure that NSF did not leak from the lumen of the silk gland, rinsed twice with 20 mM PBS
603 (pH 7.4) for 3 s each time, and then fixed in 2.5% (v/v) glutaraldehyde/phosphate buffer (0.1 M,
604 pH 7.4) (PB). Next, ASG was fixed with 1% osmium tetraoxide (OsO4) in PB buffer at 4ºC for 2
605 h after rinsed three times with PB buffer, and then dehydrated by gradient ethanol (30%, 50%,
606 70%, 80%, 90%, 100%, 100%, 7 min each) and acetone twice (10 min each). Subsequently, ASG
607 was sequentially immersed into a graded mixture of acetone and SPI-PON812 resin (19.6 mL
608 SPI-PON812, 6.6 mL DDSA, and 13.8 mL NMA) as the ratio of 3:1, 1:1, 1:3 (v/v), and then
609 infiltrated into the pure resin. Finally, ASG was embedded into the resin with 1.5% BDMA, and
610 then polymerized at 45ºC for 12 h and at 60ºC for 48 h, respectively. ASG was sliced into ultra-
611 thin sections (70 nm thick) by the ultramicrotome EM UC6 (Leica, Germany) using a diamond
612 knife, double stained with uranyl acetate and lead citrate, and then imaged on a Tecnai Spirit
613 transmission electron microscope (FEI).
614

Dynamic light scattering

616 NSF was freshly purified from PMSG with buffer II, and then centrifuged at 10,000 g for 10
617 min at 4ºC to remove the aggregates. The concentration of NSF was 0.5 mg·mL^{-1}. Dynamic light
618 scattering (DLS) was performed on NanoStar (WAYTT, USA) to determine the size distribution
619 of NSF before and after dialysis with water. The hydrodynamic radius and the polydispersity
620 coefficient were analyzed using Dynamics (ver 7.1.8.93, USA) and presented as the average
621 from ten independent tests (mean ± SD).
622

Data availability

624 All data are available in the main text or the Extended Data.
625

626 51. Q. Xia, S. Li, Q. Feng, Advances in silkworm studies accelerated by the genome sequencing of *Bombyx mori*.
627 *Annu. Rev. Entomol.* **59**, 513-536 (2014).
628 52. J. Y. Li *et al.*, Comparative proteomic analysis of the silkworm middle silk gland reveals the importance of
629 ribosome biogenesis in silk protein production. *J. Proteomics* **126**, 109-120 (2015).
630 53. T. K. Ritchie *et al.*, Chapter 11 - Reconstitution of membrane proteins in phospholipid bilayer nanodiscs.
631 *Methods Enzymol.* **464**, 211-231 (2009).
632 54. I. Wittig, H. P. Braun, H. Schagger, Blue native PAGE. *Nat. Protoc.* **1**, 418-428 (2006).
633 55. J. D. Griffith, Electron microscopic visualization of DNA in association with cellular components. *Methods Cell
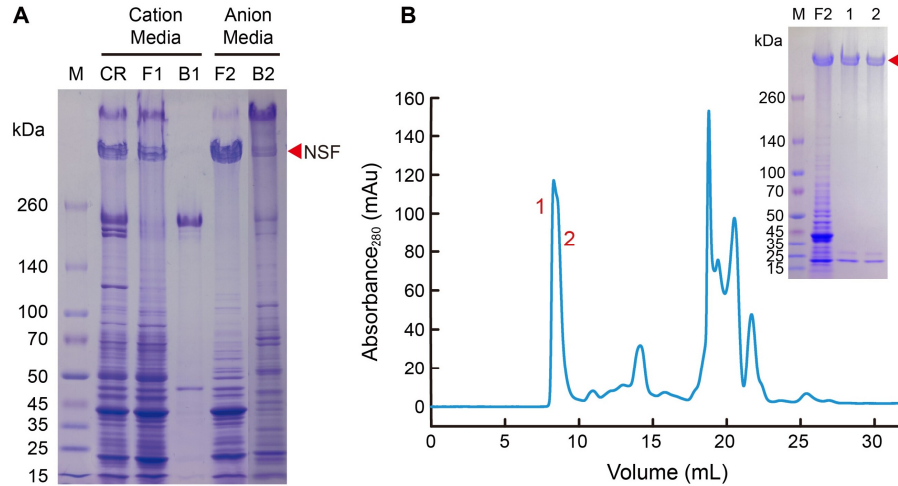634 Biol.* **7**, 129-146 (1973).
635

655
656
657
658
659
660
661
662
663
664
665
666
667
668
669
670
671
672
673
674
675
676

Extended Data Fig. 1. Identification of the subunits of NSF. (A) Identification of the subunits of NSF by a linear 4-16% gradient SDS-PAGE. **(B)** Schematic diagram of the subunits Fib-H, Fib-L, P25, P25-like. Amino acid segments identified by LC-MS/MS were indicated in red. **(C)** Typical MS/MS spectra of selected peptides matched to Fib-H, Fib-L, P25, P25-like, respectively. The peaks matched to the peptide sequences were indicated in red (b ion series) and blue (γ ion series), respectively. The unassigned peaks were gray.

Extended Data Fig. 2. Purification of NSF from ASG. (A) A linear 4-16% gradient SDS-PAGE analysis of NSF purified by ions exchange chromatography. M, marker; CR, the crude extraction of ASG; F1, flow-through fraction of the S cation exchange media; B1, beads (S); F2, flow-through fraction of the Q anion exchange media; B2, beads (Q). **(B)** Purification of NSF by size-exclusion chromatography. The inset showed the purity of NSF valued by 4-16% SDS-PAGE. Fractions 1 and 2 were pooled for CD spectra and metal shadowing.
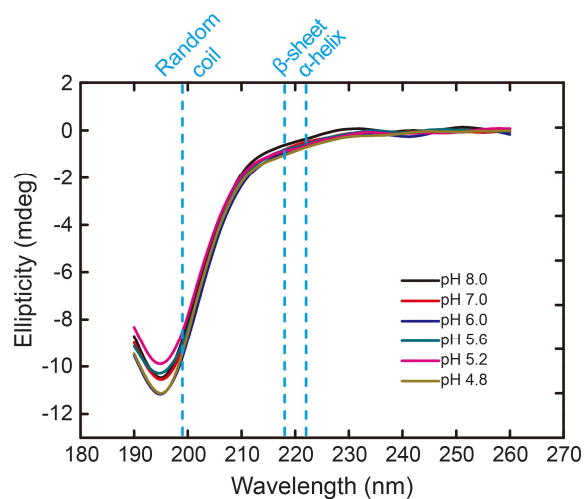
Extended Data Fig. 3. CD spectra of RSF under different pH. The concentration of RSF was 0.1 mg·mL^{-1}.
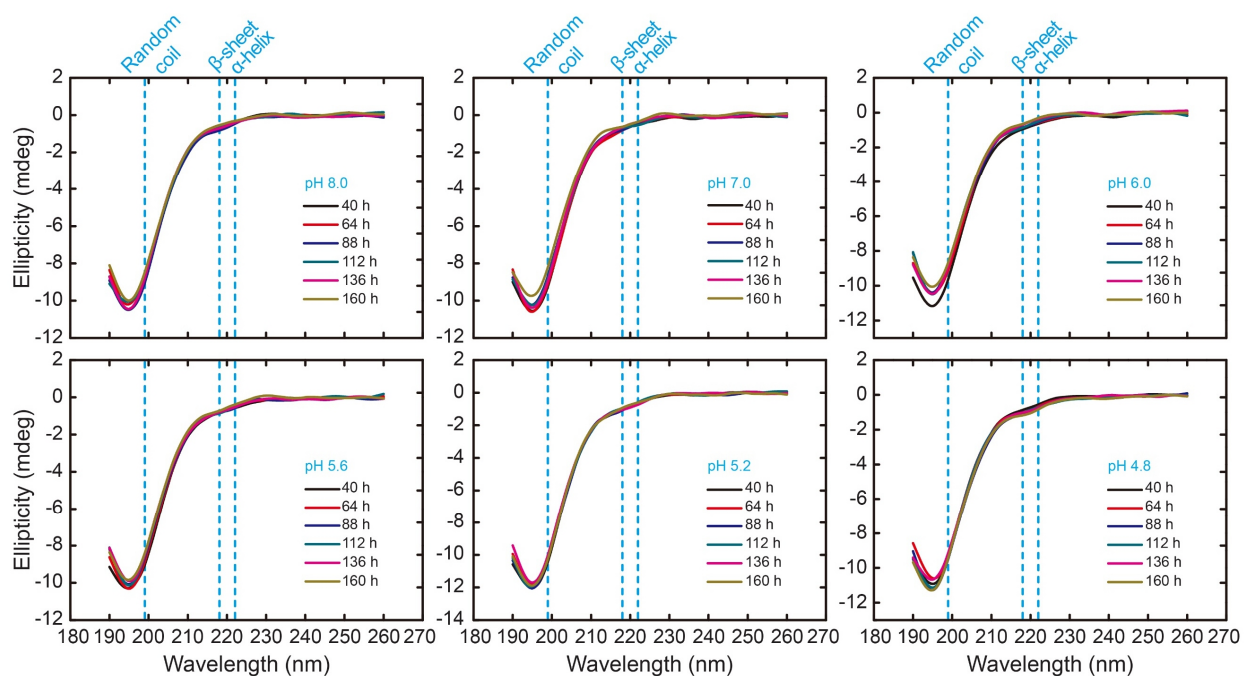
Extended Data Fig. 4. CD spectra of RSF under different pH. The concentration of RSF was 0.1 mg·mL^{-1}.

779
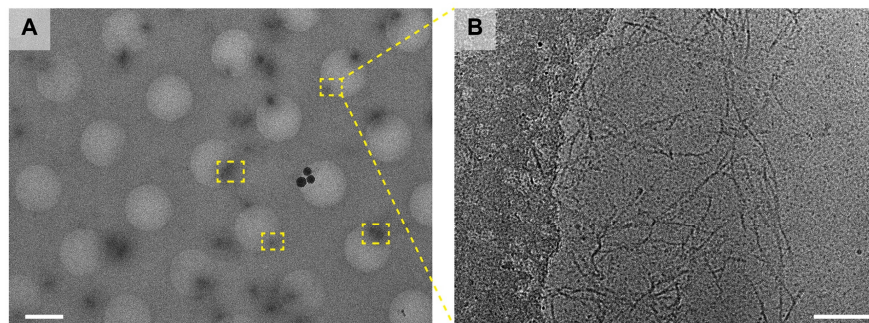
Extended Data Fig. 5. Cryo-TEM of NSF from PMSG. (A) Low-magnification image of NSF nanofibrils. Scale bar, 2 μm. **(B)** High-magnification image of NSF nanofibrils. Scale bar, 100 nm.
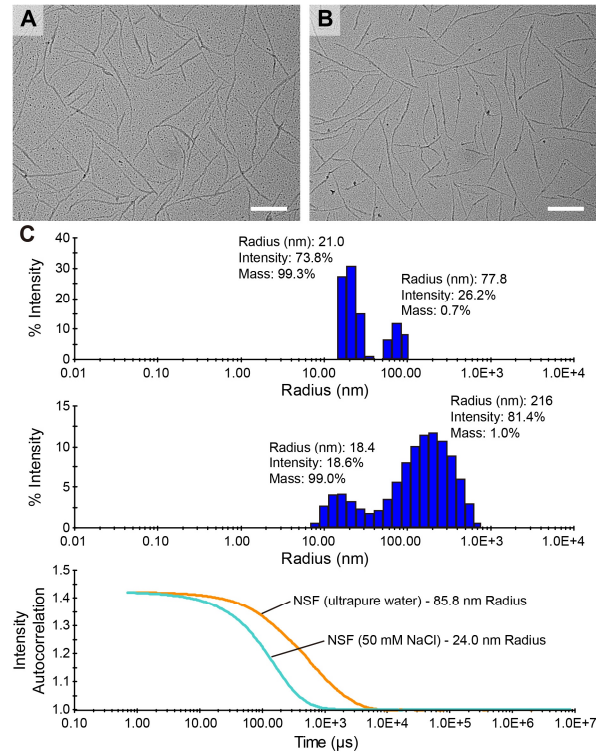
Extended Data Fig. 6. Metal shadowing of NSF. (A) Metal shadowing of NSF from PMSG. Scale bar, 200 nm. **(B)** Metal shadowing of NSF from PMSG after 18 h of incubation with 8 M urea, 2% Triton X-100, 15 mM DTT at 25°C. NSF was dissolved in buffer II with a final concentration of 0.025 mg·mL^{-1}. Scale bar, 200 nm. **(C)** DLS analysis of the hydrodynamic size distribution of NSF in buffer II (up), after dialysis against water (middle) and the correlation curves (down).
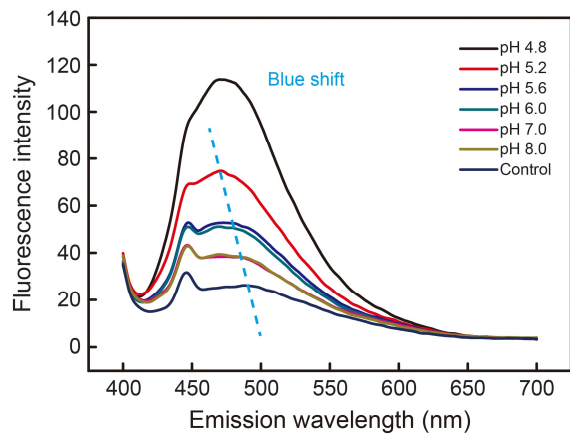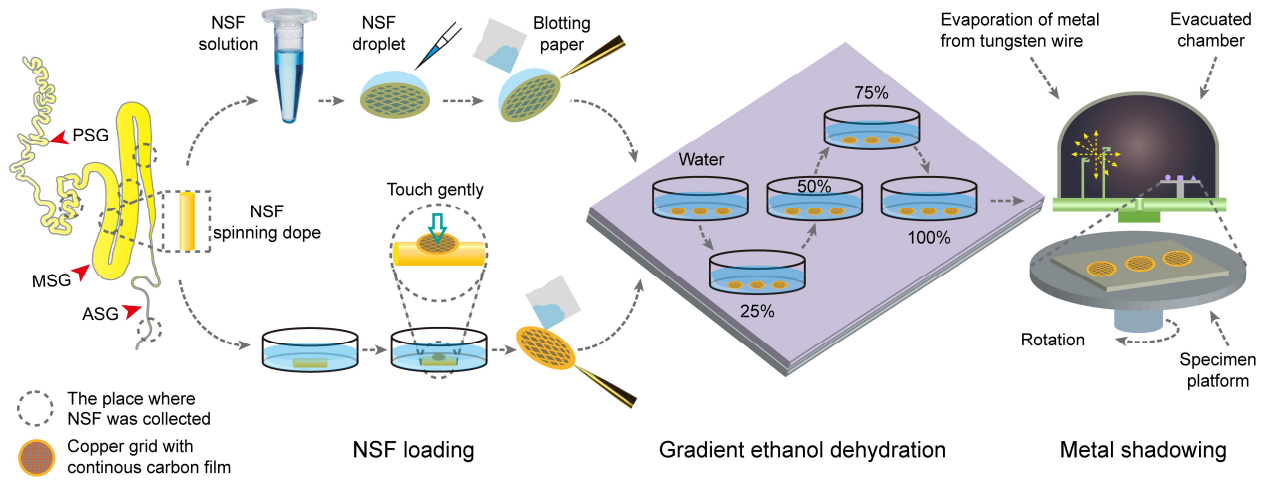
Extended Data Fig. 7. ANS fluorescence spectra of RSF under different pH. The dotted line showed the blue shift of λmax. The concentration of RSF was 0.2 mg·mL^{-1}.

877

878

Extended Data Fig. 8. Schematic diagram of the metal shadowing of NSF in water and *in situ* in the spinning dope from the silk gland.

881
882
883
884
885
886
887
888
889
890
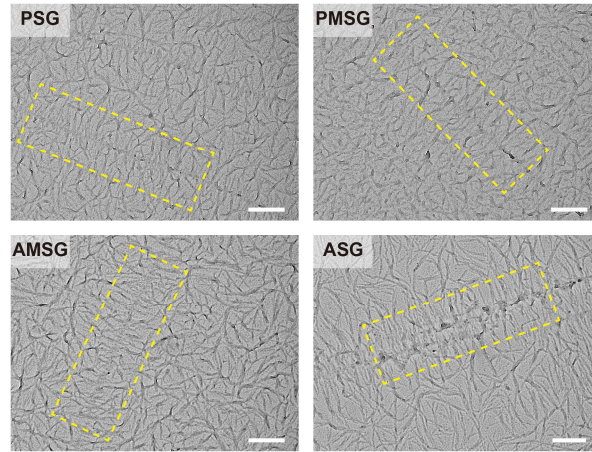891
892
893
894
895
896
897
898
899
900
901
902
903
904
905
906
907
908
909
910

Extended Data Fig. 9. Metal shadowing of NSF *in situ* in the silk gland. Dotted box represented a herringbone-like pattern of NSF nanofibrils. **PSG,** posterior silk gland. **PMSG, AMSG,** the posterior and anterior of middle silk gland, respectively. **ASG,** anterior silk gland. Scale bar, 200 nm.
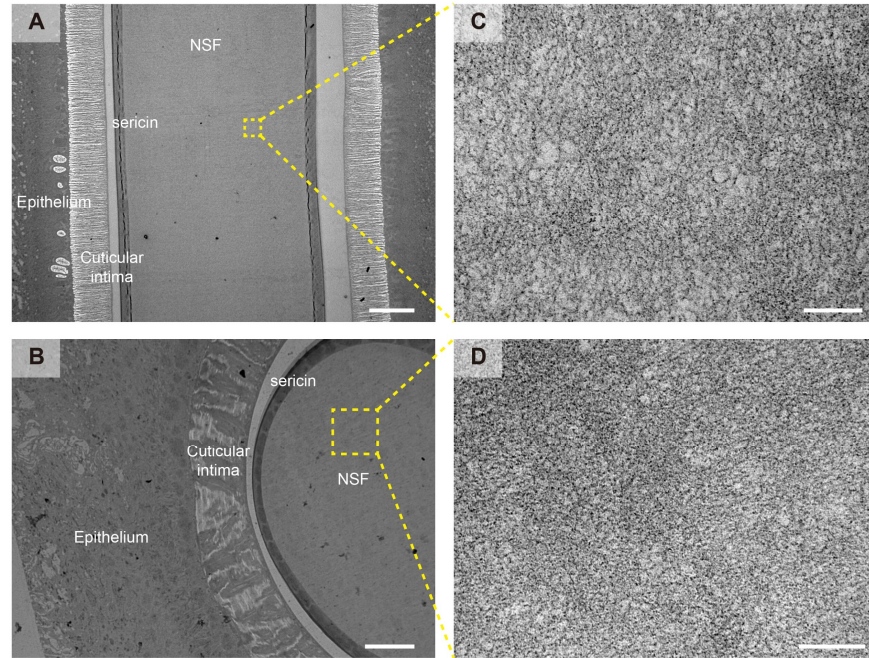
Extended Data Fig. 10. Ultrathin-section TEM of ASG-1. (A) Longitudinal section (parallel to the spinning direction) of ASG-1. Scale bar, 50 μm. **(B)** Cross-section (perpendicular to the spinning direction) of ASG-1. Scale bar, 10 μm. **(C-D)** The boxes indicated the location of the magnification, revealing the presence of isotropic NSF spinning dope in the lumen of the silk gland. Scale bar, 200 nm.

973 **Extended Data Table 1. Effect of various detergents on NSF stability**

Name	Detergent (μL)	NSF (μL)	H₂O (μL)
CHAPS (10%)	37.5	110.0	2.5
DDM (1%)	6.5	110.0	33.5
DM (100 mM)	13.5	110.0	26.5
OG (20%)	19.9	110.0	20.1
Amphipol (100 mg·mL^{-1})	13.2	110.0	26.8
5-cyclo (15%)	6.0	110.0	34.0
Digitonin (10%)	4.5	110.0	35.5
SLS (20%)	3.0	110.0	37.0
Tween-20 (3%)	10.0	110.0	30.0
Control	0.0	110.0	40.0

974
975
976
977
978
979
980
981
982
983
984
985
986
987
988
989
990
991
992
993
994
995
996
997
998
999
1000
1001
1002

1003 **Extended Data Table 2. Effect of MSP1D1 on NSF stability**

NSF:MSP1D1 (Molar ratio)	NSF (µL)	MSP1D1 (µL)	PBS (µL)
Control (1 : 0)	200.0	0.0	22.5
1 : 1	200.0	5.6	16.9
1 : 2	200.0	11.2	11.2
1 : 3	200.0	16.9	5.6
1 : 4	200.0	22.5	0.0
0 : 1	0.0	5.6	216.9
0 : 2	0.0	11.2	211.3
0 : 3	0.0	16.9	205.6
0 : 4	0.0	22.5	200.0

1004
1005
1006
1007
1008
1009
1010
1011
1012
1013
1014
1015
1016
1017
1018
1019
1020
1021
1022
1023
1024
1025
1026
1027
1028
1029
1030
1031
1032
1033

1034   **Extended Data Table 3. Effect of BSA on NSF stability**

NSF:BSA (Molar ratio)	NSF (µL)	BSA (µL)	PBS (µL)
Control (1 : 0)	200.0	0.0	22.5
1 : 1	200.0	5.6	16.9
1 : 2	200.0	11.2	11.2
1 : 3	200.0	16.9	5.6
1 : 4	200.0	22.5	0.0
0 : 1	0.0	5.6	216.9
0 : 2	0.0	11.2	211.3
0 : 3	0.0	16.9	205.6
0 : 4	0.0	22.5	200.0

1035